

Crystal and magnetic structure of the $\text{La}_{1-x}\text{Ca}_x\text{MnO}_3$ compound ($x = 0.8, 0.85$).

M. Pissas, G. Kallias

Institute of Materials Science, NCSR, Demokritos, 153 10 Aghia Paraskevi, Athens, Greece

M. Hofmann, D. M. Többens

Berlin Neutron Scattering Center, Hahn-Meitner-Institut Glienicker Str. 100 D-14109, Berlin, Germany

(Dated: February 1, 2008)

We studied the crystal and magnetic structure of the $\text{La}_{1-x}\text{Ca}_x\text{MnO}_3$ compound for $x = 0.8$ and $x = 0.85$. At $T = 300$ K both samples are paramagnetic with crystallographic symmetry $Pnma$. At low temperatures they undergo a monoclinic distortion from orthorhombic $Pnma$ -type structure with $a_p\sqrt{2} \times 2a_p \times a_p\sqrt{2}$ to a monoclinic structure with $(a_p\sqrt{2} \times 2a_p \times a_p\sqrt{2}, \beta = 90 + \varepsilon \sim 91.4^\circ)$ and $P2_1/m$ space group below T_N . The onset of the structural transformation coincides with the development of the C -type long range antiferromagnetic order with propagation vector $\mathbf{k} = (\frac{1}{2}, 0, \frac{1}{2})$. The monoclinic unit cell allowed us to determine the direction of the Mn magnetic moment with respect to the crystallographic axes: it is perpendicular to the propagation vector, $\mathbf{m} \perp \mathbf{k} = (\frac{1}{2}, 0, \frac{1}{2})$. The amplitude of the ordered magnetic moment at $T = 1.6$ K is found to be $2.53(2)$ and $2.47(2)\mu_B$ for $x = 0.8$ and 0.85 , respectively.

PACS numbers: 75.30 Vn, 25.40.Dn, 75.25.+z, 75.50.+Ee, 64.70.Kb

I. INTRODUCTION

The interest in the mixed perovskites^{1,2} $\text{La}_{1-x}\text{Ca}_x\text{MnO}_3$ has been renewed^{3,4,5,6,7,8,9,10,11,12,13,14,15,16} in connection with the discovery of colossal magnetoresistance for $x \sim 0.33$.¹⁷ For the high doping range with $x > 0.5$, the $\text{Mn}^{3+} e_g$ electrons become localized at low temperatures with a concomitant anisotropic bond reorganization in the oxygen environment of the manganoses. This cooperative atomic rearrangement can change the symmetry or not, depending upon the particular electronic concentration, orbital occupancy, average size and distribution in the La site. Thus, when the temperature is lowered through a transition temperature T_{co} , charge and orbital ordering occur. Up to now two distinct cases of charge-ordering have been reported for $x = 0.50$ and $x = 0.67$ both by transmission electron microscopy and synchrotron x-ray and neutron powder diffraction.^{18,19,20,21,22,23}

At half-doping ($x = 0.50$), the system undergoes a phase transition from paramagnetic (insulating) to ferromagnetic-metallic (FM) phase at onset temperature $T_c = 234$ K and then upon cooling to an antiferromagnetic-insulating (AFM) phase at $T_N^c = 163$ K.²⁴ The antiferromagnetic phase presents charge and spin ordered structure, called CE type¹ where real space ordering of Mn^{3+} and Mn^{4+} takes place. The basic characteristic of $x = 1/2$ phase, at low temperature, is the one after the other ordering of the Mn^{3+} and Mn^{4+} ions along the $a \approx \sqrt{2}a_p$ ($Pnma$ setting, a_p is the pseudo cubic unit cell parameter of the ideal cubic perovskite structure) leading to a superstructure with a propagation vector $\mathbf{k} = (2\pi/a)(1/2, 0, 0)$.^{18,19,20,21,25,26}

For $x = 0.67$ pioneer work of Radaelli^{22,23} and collaborators has shown a crystallographic charge-ordered^{19,20,21} and magnetic superstructure. The antiferromagnetic structure is noncollinear with the a lattice parameter to

be tripled and the c lattice parameter to be doubled with respect to the average crystallographic unit cell $Pnma$ setting. The crystallographic structure below the charge-ordering temperature ($T_{CO} \approx 260$ K) is characterized by ordering of the d_{z^2} orbitals of the Jahn-Teller-distorted Mn^{3+}O_6 octahedron in the orthorhombic ac plane, and the appearance of superlattice peaks in the x-ray patterns corresponding to a tripling of the a axis lattice parameter. The refinement has revealed ordering of the Mn^{3+} cations in sites as far apart as possible in the ac plane "Wigner-crystal" model and transverse displacements of the Mn^{4+}O_6 octahedra in the c direction. A recent study on $x = 2/3$ ²⁷ combining transmission electron microscopy with high resolution synchrotron powder x-ray diffraction data also supports the "Wigner crystal" model.

Moreover, transmission electron microscopy studies in $\text{La}_{1-x}\text{Ca}_x\text{MnO}_3$ with $x = 0.50, 0.625, 0.67, 0.75$ and 0.80 have shown superlattice reflections and their analysis pointed to a linear dependence between the magnitude of the modulation wave vector \mathbf{q}_s along the a axis and x , that is, $q_s = 1 - x$.²⁸ However, the superlattice reflections of the charge-ordering for $x = 0.8$ ^{19,28} were noticeably broader than lower compositions, indicating a very short coherence length.

Given the interplay of structural, transport, and magnetic properties on these highly correlated electron systems it is extremely important to provide information on the crystal and magnetic structure for x values above 0.75, for which the existing literature is rather limited.^{19,28}

In the present paper we discuss the crystal and magnetic structure for doping levels near the end members of the $\text{La}_{1-x}\text{Ca}_x\text{MnO}_3$ homologous series using elastic neutron diffraction data from polycrystalline $\text{La}_{1-x}\text{Ca}_x\text{MnO}_3$ samples with $x = 0.8$ and 0.85 . An important question that is been posed is whether charge

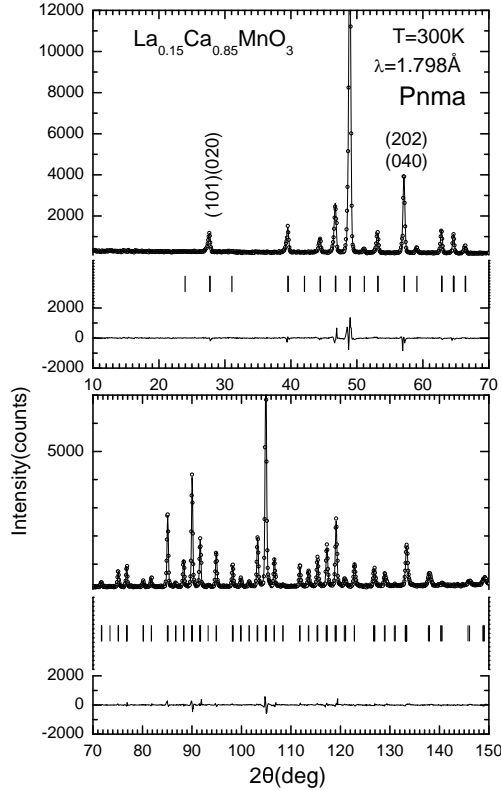


FIG. 1: Rietveld refinement for $\text{La}_{0.15}\text{Ca}_{0.85}\text{MnO}_3$ at 300 K ($\lambda = 1.798\text{\AA}$). The observed data points are indicated with open circles, while the calculated pattern is shown as a continuous line. The positions of the reflections are indicated with vertical lines below the pattern.

ordering is actually present or not.

II. EXPERIMENTAL DETAILS

$\text{La}_{1-x}\text{Ca}_x\text{MnO}_3$ samples with $x = 0.80$ and $x = 0.85$ were prepared by thoroughly mixing high purity stoichiometric amounts of CaCO_3 , La_2O_3 , and MnO_2 . The mixed powders reacted in air in temperatures up to 1400°C for several days with intermediate grindings. Finally the sample was slowly cooled to room temperature. Neutron diffraction data were collected on the E6 and E9 diffractometers of the research reactor BER II in Berlin. The neutron powder diffraction experiments as a function of temperature in the low angle range were performed in diffractometer E6 using a wavelength $\lambda = 2.44\text{\AA}$ ((002) reflection of a pyrolytic graphite monochromator). For crystal structure refinement, data were collected on the E9 diffractometer with wave length $\lambda = 1.798\text{\AA}$ ((511) reflection of a vertically focusing Ge monochromator), with collimation $\alpha_1 = 10^\circ$ (in pile collimator), $\alpha_2 = 20^\circ$ (second collimator after monochromator) and $64 \times 10^\circ$ collimators in front of 64 ^3He single detector tubes. The powdered samples were placed in

a cylindrical vanadium can ($D = 8\text{ mm}$) mounted in an ILL orange cryostat. DC magnetization measurements were performed in a superconducting quantum interference device (SQUID) magnetometer (Quantum Design).

III. CRYSTAL STRUCTURE

We performed Rietveld refinements of the nuclear and magnetic structures of neutron data using the FULLPROF program.²⁹ The systematically absent reflections of the $x = 0.8, 0.85$ diffraction patterns at 300 K are consistent with space group $Pnma$. The crystal structure at 300 K was refined using as starting model the orthorhombic GdFeO_3 type structural model. First, the scale factor, background, unit cell parameters and zero-shift errors were optimized. The peak shapes are well described by function proposed by Finger, Cox and Jephcoat³⁰ in order to model appropriately the high vertical apertures used in the beam geometry.³¹ Then, we refined the atomic positions and the isotropic thermal parameters. In the final step, we refined the oxygen thermal parameters anisotropically reducing further the refinement agreement parameters. Figure 1 shows as an example the observed and calculated neutron powder diffraction intensity patterns for the $\text{La}_{0.15}\text{Ca}_{0.85}\text{MnO}_3$ sample at 300 K. The corresponding structural parameters are reported in Table I and the selected bond distances in Table II. The structure at this temperature is orthorhombic with $a > c > b/\sqrt{2}$. Assuming that the Mn site is completely occupied and refining the occupation factors for La/Ca and O we found the nominal ones within the standard deviation errors. Judging from the estimated Mn-O distances, the octahedral distortion is small and can be considered as slightly tetragonally elongated with four short bonds $\sim 1.91\text{\AA}$ (two in the basal plane ($a - c$ -plane) and two apical bond (along b -axis)) and two longer bonds $\sim 1.92\text{\AA}$ in the basal plane.

The neutron diffraction patterns, below a temperature denoted by T_c , indicate a change of symmetry since several extra peaks appear with respect to the high temperature $Pnma$ space group. Figure 2 shows the neutron diffraction patterns collected with a wavelength 2.44\AA (E6 diffractometer) for the $x = 0.85$ sample from $T = 1.6$ K up to 165 K. Close inspection of the diffraction pattern at $T = 1.6$ K shows a splitting of the (111) reflection, characteristic for the existence of monoclinic distortion of the structure with the monoclinic angle $\beta > 90^\circ$. In the case of a monoclinic distortion of the unit cell, one expects a splitting of the reflections (111) and $(\bar{1}11), (d^{-2}(\bar{1}11) - d^{-2}(111) \propto -\cos \beta)$, since the cross term hl in the expression for the d-spacing for these reflections is non zero.

The structure at $T = 300$ K is associated with the $\text{GdFeO}_3/\text{CaTiO}_3$ type structures (like the samples with different Ca content) and is derived from the cubic perovskite by a combination of MnO_6 octahedra tilts (Glazer³² notation $Pnma$, $a^-b^+a^-$). Looking in

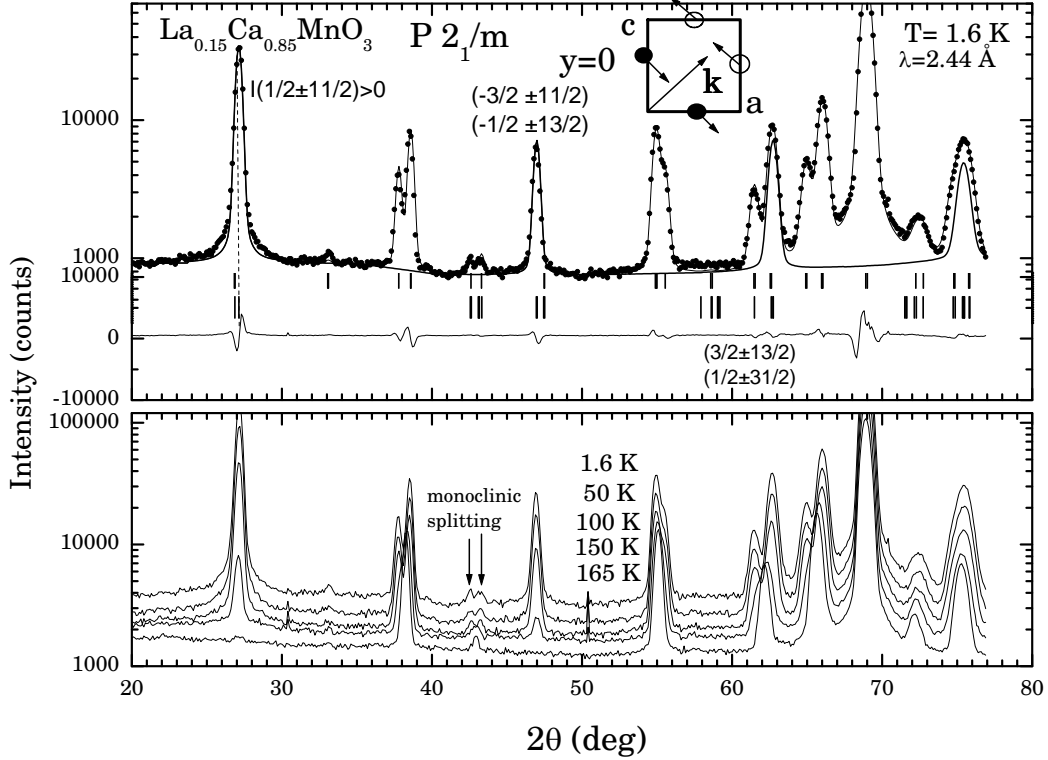


FIG. 2: Observed and calculated neutron powder diffraction intensity patterns at $T = 1.6$ K and neutron diffraction patterns at 50 K, 100 K, 150 K and 165 K of the $\text{La}_{0.15}\text{Ca}_{0.85}\text{MnO}_3$ sample ($\lambda = 2.44\text{\AA}$). The observed data points are indicated with solid circles, while the total structural and magnetic calculated pattern are shown as continuous lines. The positions of the reflections for the crystal and magnetic structure employed in the refinements are indicated with vertical lines below the pattern. The indices refer to the magnetic reflections. The splitting of the (111) reflection (at 43 degrees) due to the monoclinic distortion can also be seen.

Glazer's classification for an octahedral tilt system which maintains the tilt system $a^-b^+a^-$ and is compatible with a monoclinic unit cell, we selected the tilt system $a^-b^+c^-$ to refine the low temperature monoclinic phase. This tilt system is described with the monoclinic space group $P2_1/m$, which is a subgroup of $Pnma$. In $P2_1/m$ space group there are two non-equivalent sites for La and Mn.³³ Each Mn site has its own apical oxygen (bond direction mainly along b -axis). Concerning the two plane oxygens at the general position they are shared by the two Mn sites. In order to reduce the free parameters we used the constraints $B(\text{La}(1)) = B(\text{La}(2))$ and $B(\text{Mn}(1)) = B(\text{Mn}(2))$ for La and Mn temperature factors respectively. The refinement of neutron diffraction patterns after taken the above constraints into consideration gives very good Rietveld agreement factors. The same type of monoclinic distortion has been observed in $\text{Sm}_{0.15}\text{Ca}_{0.85}\text{MnO}_3$ and $\text{Bi}_{0.15}\text{Ca}_{0.85}\text{MnO}_3$ compounds.^{34,35} Due to the low x-ray scattering factor of oxygen the experiments done by Zheng et al.³⁶ were not sensitive enough to find the correct structural transition in $\text{La}_{0.17}\text{Ca}_{0.83}\text{MnO}_3$.

We have also tested the space group $P2_1/n$ (No 14)

which follows the tilt system $a^-b^-c^-$ with an 1 : 1 ordering of the Mn ions.³³ However, this model is not able to account for the peak at $2\theta \simeq 43.5^\circ$, as well as for several other peaks at the high angles. We were therefore led to rule out this possibility. Recently Lobanov et al.³⁷ reported that the ferromagnetic insulated $\text{La}_{0.85}\text{Ca}_{0.15}\text{MnO}_3$ compound undergoes a monoclinic distortion below the ferromagnetic transition (space group $P2_1/c$) with nonequivalent MnO_2 layers alternating along the a axis. In their model they considered that the monoclinic angle is between the b and c axis of the high temperature $Pnma$ structure. From the specific pattern of Mn-O distances they proposed an unconventional orbital ordering. We tested also this model but since it does not predict splitting of the (202) reflection it can not account for the low temperature diffraction pattern of $\text{La}_{0.15}\text{Ca}_{0.85}\text{MnO}_3$. Figure 3 shows the observed and calculated neutron powder diffraction intensity patterns for $\text{La}_{0.15}\text{Ca}_{0.85}\text{MnO}_3$ at 1.6 K (the plot for $x = 0.8$ was similar) using neutron diffraction data from E9 diffractometer. The corresponding structural parameters for both samples are reported in Table I and the selected bond distances in Table II. The bonds' length

TABLE I: $\text{La}_{1-x}\text{Ca}_x\text{MnO}_3$ ($x = 0.8$ and 0.85) structural parameters at $T = 300$ and 1.6 K as determined from Rietveld refinements based on neutron powder diffraction data of the E9 diffractometer ($\lambda = 1.798\text{\AA}$). The space group $Pnma$ (No62) was used for the data at $T = 300$ K. La, Ca and apical oxygen (Oa) occupy the $4c$, $(x, 1/4, z)$ site, Mn the $4b$ $(0, 0, 1/2)$ site and the plane oxygen (Op) the general $8d$ site. The monoclinic space group $P2_1/m$ (b axis unique No 11) was used for the data at $T = 1.6$ K. The atomic sites for $P2_1/m$ are: La/Ca $1,2$, Oa $1,2$ $2e[x, \frac{1}{4}, z]$, Mn 1 $2b[\frac{1}{2}, 0, 0]$, Mn 2 $2c[0, 0, \frac{1}{2}]$, and Op $1,2$ $4f[x, y, z]$. The parameters U_{ij} represent the eigenvalues of the cartesian U -matrix. Numbers in parentheses are statistical errors referring to the last significant digit.

x	0.8		0.85	
T (K)	300	1.6	300	1.6
a (\text{\AA})	5.3386(1)	5.3529(2)	5.3243(1)	5.3356(1)
b (\text{\AA})	7.5376(1)	7.4648(3)	7.5193(1)	7.4596(1)
c (\text{\AA})	5.3367(1)	5.3506(2)	5.3189(1)	5.3258(1)
β°	90	91.502(2)	90	91.141(1)
La1 x	0.0240(7)	0.022(2)	0.0247(7)	0.029(1)
z	-0.006(1)	-0.005(1)	-0.009(1)	-0.005(1)
B (\text{\AA}^2)	1.13(6)	0.79(7)	0.89(6)	0.70(5)
La2 x		0.522(2)		0.528(1)
z		0.509(2)		0.509(1)
B		0.81(7)		0.70(5)
Mn1 B	0.80(7)	0.43(7)	0.49(6)	0.37(6)
Mn2 B	-	0.43(7)	-	0.37(6)
O1a x	0.4921(8)	0.497(2)	0.4913(7)	0.495(1)
z	0.063(1)	0.061(1)	0.061(1)	0.061(1)
U_{11} (\text{\AA}^2)	0.014(4)	0.006(3)	0.013(6)	0.015(1)
U_{22}	0.0041(3)	0.001(1)	0.008(7)	0.002(1)
U_{33}	0.0095(4)	0.011(1)	0.010(4)	0.010(2)
O2a x		0.988(2)		0.985(1)
z		0.438(1)		0.434(1)
U_{11}		0.006(3)		0.015(3)
U_{22}		0.001(1)		0.002(1)
U_{33}		0.011(1)		0.010(3)
O1p x	0.2827(7)	0.282(1)	0.2828(6)	0.2829(8)
y	0.0414(4)	0.038(1)	0.0338(5)	0.0342(8)
z	0.7155(8)	0.721(1)	0.7151(7)	0.7198(9)
U_{11}	0.0075(3)	0.022(2)	0.0001	0.011(2)
U_{22}	0.0114(8)	0.006(1)	0.01638	0.003(1)
U_{33}	0.0202(5)	0.003(1)	0.0174	0.007(5)
O2p x		0.781(1)		0.7842(8)
y		0.028(1)		0.0308(6)
z		0.779(1)		0.782(1)
U_{11}		0.022(2)		0.011(2)
U_{22}		0.006(1)		0.003(1)
U_{33}		0.003(1)		0.007(1)
R_p	6.86	7.7	6.9	6.60
R_{wp}	9.25	9.9	9.7	9.21
R_B	6.35	4.86	5.09	4.82
μ_x		1.79(1)		1.73(1)
μ_z		-1.79(1)		-1.73(1)
μ		2.53(2)		2.47(2)
$R_B(m)$		6.8		6.59

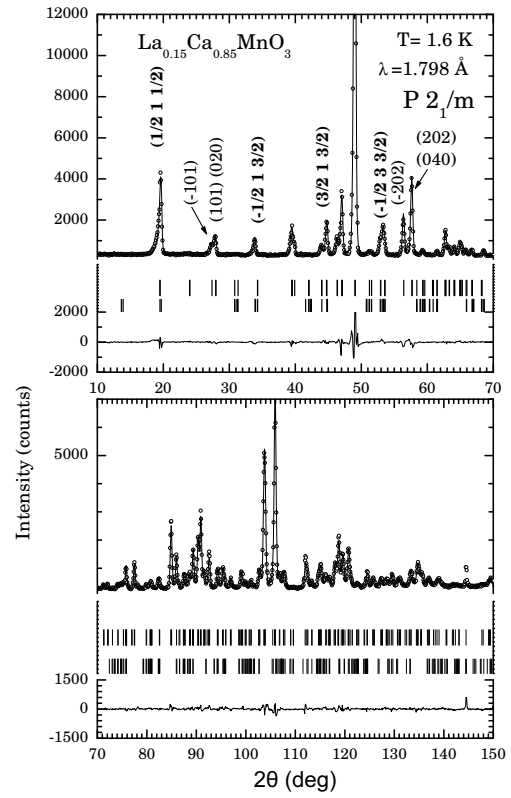


FIG. 3: Rietveld refinement pattern for $\text{La}_{0.15}\text{Ca}_{0.85}\text{MnO}_3$ at 1.6 K ($\lambda = 1.798\text{\AA}$). The observed data points are indicated with open circles, while the calculated pattern is shown as a continuous line. The positions of the reflections for the crystal and magnetic structure employed in the refinements are indicated with vertical lines below the pattern.

at $T = 1.6$ K shows that the Mn(1) site has two long bonds with O2p (~ 1.94 \text{\AA} for $x = 0.85$) in the $a - c$ plane and four short averaging to ~ 1.88 \text{\AA}.

In $\text{LaMn}^{3+}\text{O}_3$ (which is a pure Mn^{+3} compound) the Mn^{+3}O_6 octahedra display a large JT distortion and coherent orbital ordering, with two long in-plane Mn^{+3}O bonds (2.181\AA) and four short (2×1.914 \text{\AA} in-plane and 2×1.966 \text{\AA} along the b axis).³⁸ Upon substitution of Ca for La in the metallic ferromagnetic or insulating paramagnetic state the MnO_6 octahedra have six almost equal bond length $\sim 1.951\text{\AA}$.³⁹ In the case of $\text{La}_{0.5}\text{Ca}_{0.5}\text{MnO}_3$ and in the charge-ordered state the structure has two sites with characteristics of Mn^{+3} and Mn^{+4} , respectively. The Mn^{+3}O_6 octahedra have two in-plane long bonds ~ 2.07 \text{\AA} and four short ~ 1.92 \text{\AA}. On the other hand the Mn^{+4}O_6 octahedra have six short almost equidistant bonds $\sim 1.91\text{\AA}$.¹⁸ The same occurs in the $\text{La}_{0.33}\text{Ca}_{0.67}\text{MnO}_3$ compound in the charge-ordered state, with the Mn^{+3}O_6 octahedra being JT distorted ($2 \times 2.02\text{\AA}$ and $4 \times 1.91\text{\AA}$) and the Mn^{+4}O_6 octahedra having five short bonds ($\sim 1.9\text{\AA}$) except for a single long bond ($\sim 2.0\text{\AA}$) attributed to the frustrated Mn-O-Mn interaction.²²

The main effect of the transition at T_c is a redistribution of the Mn-O bond lengths, rather than that of the bond angles. At room temperature, the octahedral coordination of manganese with oxygen is approximately undistorted, with four short bonds $\sim 1.91\text{\AA}$ (two in the basal plane and two along b -axis) and two longer bonds $\sim 1.92\text{\AA}$ in the basal plane. Upon cooling below T_c , the structural changes are evident in the MnO_6 octahedra. The two crystallographically independent MnO_6 octahedra are tetragonally elongated with the two Mn-O $2p$ bonds in the $a - c$ plane elongated and four short bonds (Mn- O_p and Mn- O_a) along the b -axis and $a - c$ plane respectively. This is also the manifestation of the static Jahn-Teller effect. The two manganese sites present in the monoclinic phase have very similar environments, except for the distortion parameter (see Table II) which is different by one order of magnitude. This fact may imply that the monoclinic phase displays orbital ordering but it does not show the typical signature of charge ordering. This orbital ordering is developed concomitantly with the antiferromagnetic ordering (see next section). Due to absence of large local distortions in the MnO_6 octahedra one can say that the high temperature phase undergoes a homogeneous distortion at $T = T_c$ and in the low temperature monoclinic structure the e_g electrons are not definitely localized (absence of charge ordering). At this point we must note that the charge ordering model can not rule out completely because, the difference in the structural parameters for the charge ordering model at the studied concentrations ($x = 0.8, 0.85$) may be small.

The presence of two long bonds for both Mn sites at the monoclinic phase is a result of the fact that the e_g electrons are σ -antibonding and any localization or confinement of them to a specific plane or direction will result in an expansion of the bonds in that directions. Delocalization of the e_g electrons should lead to a very isotropic distribution of Mn-O distances in agreement with our observation above T_c .

Figure 4 shows the variation of the lattice parameters $a, b/\sqrt{2}$ and c with temperature for both samples. The lattice parameters display changes below T_{\max} . The b -axis undergoes a drastic decreasing while the a and c axes slightly increase. Since $a > c > b/\sqrt{2}$ the $x = 0.8$ and 0.85 samples belong to the so-called O' structure. This type of structure can result from octahedral tilting and a cooperative JT distortion (orbital ordering). For comparison we include in this figure the temperature variation of the magnetic moment deduced from the SQUID measurements during warming, for both samples (see right scale). Both measurements display a maximum at $T_{\max} = 210$ K and 160 K for $x = 0.8$ and 0.85 samples, respectively. The observed magnetization peak can be explained by considering that at high temperatures the hopping of the e_g electron induces ferromagnetic correlations through the double-exchange mechanism and when these electrons freeze the ferromagnetic fluctuations are replaced by superexchange driven antiferromagnetic spin fluctuations. Figure 5 shows the variation of the mon-

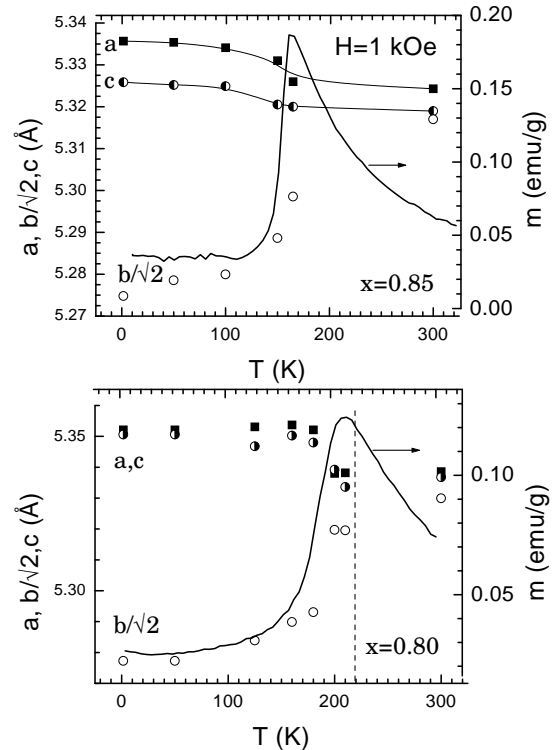


FIG. 4: Lattice parameters as a function of temperature for $\text{La}_{1-x}\text{Ca}_x\text{MnO}_3$ ($x = 0.8$ (lower panel) and $x = 0.85$ (upper panel)) as obtained from the neutron diffraction data. Error bars are smaller than the symbols. The bold continuous line represents the magnetic moment measured after zero field cooling during warming under a 1 kOe magnetic field.

oclinic angle β as a function of temperature for both samples. In the same plot we include the temperature variation of the ordered magnetic moment per Mn ion (deduced from the magnetic peak intensity in neutron diffraction, see next section) for both samples. The monoclinic angle increases from 90° at T_c to $\sim 91^\circ$ at low temperatures and follows the temperature variation of the ordered magnetic moment shown in fig. 5. Also, the transition point marked by the appearance of the monoclinic distortion coincides with the peak observed in the SQUID data (fig. 4). The space group describing the low temperature structure is a maximal subgroup of the high temperature phase. Then, according the Landau theory⁴⁰ of phase transitions one expect that the transition is of second order. In other words it is possible to go from the $Pnma$ structure to $P2_1/m$ by a continuous change in the cation displacements.

Finally, we discuss the possibility that the Mn(2) sites are occupied exclusively by Mn^{+4} ions. The Mn(1) sites with longest bond length $\sim 1.95\text{\AA}$ ($x = 0.80$ sample) corresponds to a site with a Mn^{+3} character. For example it can be considered as randomly occupied by 60% Mn^{+4} and 40% Mn^{+3} . Of course the Mn^{+4} -O bond length is

shorter by $\sim 0.05\text{\AA}$ in comparison with $x = 0.5$ or $2/3$. The distortion is smaller for the sample with $x = 0.85$ than for that with $x = 0.80$. Therefore, we might conclude that if at $x = 0.75$ a clear charge-ordered state exists then when Ca content is further increased, the crystal is tending more and more to acquire the structure of CaMnO_3 with a homogeneous distortion of the $T = 300\text{ K }Pnma$ phase.

A. Magnetic structure

In this section we will discuss the magnetic reflections appearing at $T < T_c$ using neutron diffraction data from the E6 diffractometer. Figure 2 shows the neutron diffraction patterns of the $\text{La}_{0.15}\text{Ca}_{0.85}\text{MnO}_3$ sample recorded with $\lambda = 2.44\text{\AA}$ in the range $1.6 - 165\text{ K}$. Below $T_c = 150\text{ K}$ splitting of the family of peaks $[(101), (020)]$ and (111) due to the monoclinic distortion is observed. A series of additional Bragg peaks occurring mainly at low angles give a clear indication for the presence of antiferromagnetic long-range ordering. The antiferromagnetic ordering occurs concomitantly with the monoclinic

transition at T_c ($T_N = T_c$). All the magnetic peaks can be indexed using the propagation vector $\mathbf{k} = [\frac{1}{2}, 0, \frac{1}{2}]$ (U point of the first Brillouin zone). The magnetic structure for this propagation vector corresponds to the so-called type-C antiferromagnetic structure.^{1,22}

The integrated intensity of a magnetic reflection at $\mathbf{q} = \mathbf{Q} + \mathbf{k}$ (\mathbf{Q} is a reciprocal lattice vector) for a collinear magnetic structure in a neutron powder diffraction pattern can be written as:

$$I(\mathbf{q}) = \frac{I_0}{V^2 \sin \theta \sin 2\theta} m \langle 1 - (\hat{\mathbf{q}} \cdot \hat{\mathbf{s}})^2 \rangle |F(\mathbf{q})|^2 \quad (1)$$

where I_0 is the scale factor, V is the unit cell volume, θ is the Bragg angle and m is the multiplicity of the reflection \mathbf{q} . The term $\langle 1 - (\hat{\mathbf{q}} \cdot \hat{\mathbf{s}})^2 \rangle$ is an average over all the equivalent $\{\mathbf{q}\}$ reflections, $\hat{\mathbf{q}}$ is the unit scattering vector, $\hat{\mathbf{s}}$ is the unit vector along the axis of the collinear magnetic structure and $F(\mathbf{q})$ is the magnetic structure factor for the configurational symmetry. The magnetic structure factor for the particular crystal and magnetic structure can be written as

$$F(\mathbf{q}) = \{1 - \exp(\pi i k)\} \left\{ p_1 \exp \left[\pi i \left(h + \frac{1}{2} \right) \right] + p_2 \exp \left[\pi i \left(l + \frac{1}{2} \right) \right] \right\} \quad (2)$$

where $p_j = (0.269 \times 10^{-12} \text{ cm}/\mu_B) \times S_1 \times f_j \times \exp(-W_j)$, S_1 (S_2) is the average ordered magnetic moment in Bohr magnetons μ_B for the Mn ion at $(1/2, 0, 0)$ site $((0, 0, 1/2))$, f_j is the magnetic form factor for the Mn ion and W_j is the Debye-Waller factor for the j th Mn ion. Thanks to the monoclinic distortion the diffraction pattern revealed zero intensity for the resolved reflections $(\frac{1}{2}, \pm 1, -\frac{1}{2})$ and $(\frac{3}{2}, \pm 1, \frac{1}{2}), (\frac{1}{2}, \pm 1, \frac{3}{2})$. Using Eq. 2 we can readily conclude that $p_1 = p_2$. The ferromagnetic interactions occur along the two long in-plane Mn-O bonds, while along the four short Mn-O bonds the interactions are antiferromagnetic. The relative intensity of the reflections $(\frac{1}{2}, \pm 1, \frac{1}{2})$ and $(-\frac{3}{2}, \pm 1, \frac{1}{2}), (-\frac{1}{2}, \pm 1, \frac{3}{2})$ implies that $\mathbf{S} \perp \mathbf{k}$, that is, the magnetic moment is directed along the two long in-plane Mn-O bonds. The fit of the experimental pattern at $T = 1.6\text{ K}$ gives an amplitude for the ordered magnetic moment per Mn ion of $2.53(2)$ and $2.47(1)\mu_B$ for $x = 0.8$ and 0.85 , respectively. These values are smaller than the theoretically expected for the stoichiometric mixtures of Mn^{+4} and Mn^{+3} (e.g. $0.15 \times 4 + 0.85 \times 3 = 3.15$). The smaller observed magnetic moment than their nominal value of random mixture indicate the hybridization of the Mn t_{2g} orbitals and the O $2p$ orbitals. The temperature variation of the ordered magnetic moment per Mn ion as obtained from Rietveld refinement of the neutron powder diffraction data

for both samples is plotted in Fig 4.

IV. CONCLUSIONS

The present work based on the analysis of neutron powder diffraction data shows that $x = 0.80$ and $x = 0.85$ undergo an orthorombic-to-monoclinic structural transition around 210 K and 160 K , respectively. The monoclinic distortion is larger for the $x = 0.80$ sample. Simultaneously, long range antiferromagnetic order is developed and it can be described with propagation vector $\mathbf{k} = [\frac{1}{2}, 0, \frac{1}{2}]$ that corresponds to the C-type structure. The ordered magnetic moment of the Mn ions is found to be normal to the propagation vector.

A key question was about the existence or not of charge-ordering at low temperatures. Charge-ordering models without or with monoclinic distortions have failed to refine the diffraction patterns. The refinement was successful only with the $P2_1/m$ space group, where the two Mn sites in the low temperature structure have similar environments (in terms of their bond lengths in the corresponding MnO_6 octahedra). This absence of preferential local distortions (which would be a sign of different charges in the two Mn sites) in the MnO_6 octahedra have led us to conclude that charge-ordering does not

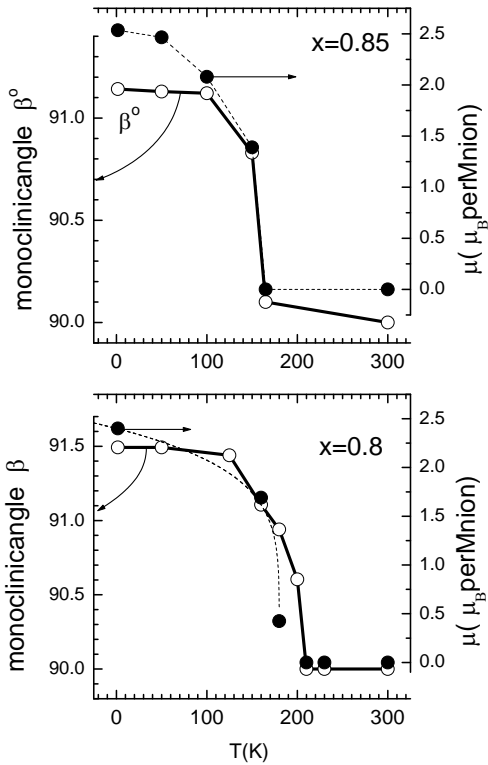


FIG. 5: Monoclinic angle β and ordered magnetic moment per Mn ion as a function of temperature for $\text{La}_{1-x}\text{Ca}_x\text{MnO}_3$ ($x = 0.8, 0.85$) as obtained from the neutron diffraction data. The continuous lines are guides for the eye. Error bars are smaller than the symbols.

occur in the monoclinic phase. However, the difference in the structural parameters for charge-order and charge disorder of Mn^{+3} and Mn^{+4} with ratios of $0.15 : 0.85$ and $0.2 : 0.8$ may be as small (or smaller) as the sensitivity of the experimental method.

Acknowledgments

This work was partially supported from the Greek Secretariat for Research and Technology through the PENED program 99ED186 and by the EC through the CHRX-CT93-0116 access to large-scale facilities project.

- ¹ E. O. Wollan and W. C. Koehler, Phys. Rev. **100**, 545 (1955).
- ² J. B. Goudenough, Phys. Rev. **100**, 564 (1955).
- ³ P. Schiffer, A. P. Ramirez, W. Bao, and S.-W. Cheong, Phys. Rev. Lett. **75**, 3336 (1995).
- ⁴ H. Kuwahara, Y. Tomioka, A. Asamitsu, Y. Moritomo, and Y. Tokura, Science **270**, 961 (1995).
- ⁵ Y. Tomioka, A. Asamitsu, Y. Moritomo, H. Kuwahara, and Y. Tokura, Phys. Rev. Lett. **71**, 5108 (1995).
- ⁶ J. W. Lynn, R.W. Erwin, J. A. Borchers, Q. Huang, A. Santoro, J-L. Peng and Z. Y. Li, Phys. Rev. Lett. **76**, 4046 (1996).
- ⁷ A. P. Ramirez, P. Schiffer, S.-W. Cheong, C. H. Chen, W. Bao, T. T. Palstra, P. L. Gammel, D. J. Bishop, and B. Zegarski, Phys. Rev. Lett. **76**, 3188 (1996).
- ⁸ S. Satpathy, Z. S. Popovic, and F. R. Vukajlovic, Phys. Rev. Lett. **76**, 960 (1996).
- ⁹ A. J. Millis, Nature **392**, 147 (1998).
- ¹⁰ E. L. Nagaev, Usp. Fiz. Nauk **166**, 833 (1996); E. L. Nagaev, Physics-Uspekhi **39**, 781 (1996).
- ¹¹ P. Majumdar and P. Littlewood Phys. Rev. Lett. **81**, 1314 (1998).
- ¹² A. Moreo, S. Yunoki, and E. Dagotto, Science **283**, 2034 (1999).
- ¹³ G. Varelogiannis, Phys. Rev. Lett. **85**, 4172 (2000).
- ¹⁴ A. P. Ramirez, J. Phys.: Condens. Matter **9**, 8171 (1997).
- ¹⁵ C. N. R. Rao, Anthony Arulraj, A. K. Cheetham and Bernard Raveau, J Phys.:Condens. Matter **12**, 83 (2000).
- ¹⁶ M. Pissas, G. Kallias, E. Devlin, A. Simopoulos, and D. Niarchos, J. Appl. Phys. **81**, 8 (1997).
- ¹⁷ R. von Helmolt, J. Wecker, B. Holzapfel, L. Schultz, and K. Samwer, Phys. Rev. Lett. **71**, 2331 (1993).
- ¹⁸ P. G. Radaelli, D. E. Cox, M. Marezio, and S-W. Cheong, Phys. Rev. B **55**, 3015 (1997); P. G. Radaelli, G. Iannone, M. Marezio, H. Y. Hwang, S-W. Cheong, J. D. Jorgensen, and A. N. Argyriou, Phys. Rev. B **56**, 8265 (1997).
- ¹⁹ C. H. Chen and S-W. Cheong, Phys. Rev. Lett. **76**, 4042 (1996); C. H. Chen, S-W. Cheong, and H. Y. Hwang, J. Appl. Phys. **81**, 4326 (1997).
- ²⁰ S. Mori, C. H. Chen, and S.-W. Cheong, Nature **492**, 473 (1998).
- ²¹ S. Mori, C. H. Chen, and S-W. Cheong, Phys. Rev. Lett. **81**, 3972 (1998).
- ²² P. G. Radaelli, D. E. Cox, L. Capogna, S-W. Cheong, and M. Marezio, Phys. Rev. B **59**, 14440 (1999).
- ²³ M. T. Fernandez-Diaz, J. L. Martinez, and J. M. Alonso E. Herrero, Phys. Rev. B **59**, 1277 (1999).
- ²⁴ M. Roy, J. F. Mitchell, A. P. Ramirez, P. Schiffer, Phys.

Rev. B **58**, 5185 (1998); W. Cheong, P. E. Schiffer, and A. P. Ramirez, Phys. Rev. Lett. **75**, 4488 (1995).

²⁵ G. Kallias, M. Pissas and A. Hoser, Physica B **276-278**, 778 (2000).

²⁶ Q. Huang, J. W. Lynn, R. W. Erwin, A. Santoro, D. C. Dender, V. N. Smolyaninova, K. Ghosh, and R. L. Greene, Phys. Rev. B, **61**, 8895 (2000).

²⁷ Renhui Wang, Jianian Gui, Yimei Zhu, and A. R. Moodenbaugh, Phys. Rev. B **61**, 11946 (2000).

²⁸ J. Q. Li, M. Uehara, C. Tsuruta, Y. Matsui, and Z. X. Zhao.

²⁹ J. Rodriguez-Carvajal, Physica B **192**, 55 (1993).

³⁰ L. W. Finger, D. E. Cox, A. P. Jephcoat, J. Appl. Cryst. **27**, 892 (1994).

³¹ D. M. Többens, N. Stüsser, K. Knorr, H. M. Mayer, G. Lampert, Mater. Sci. Forum in press.

³² A. M. Glazer, Acta Cryst. **B28**, 3384 (1972).

³³ P. M. Woodward, Acta Cryst. **B53**, 32 (1997).

³⁴ C. Martin, A. Maignan, M. Hervieu, B. Raveau, Z. Jirák, A. Kurbakov, V. Trounov, G. André, F. Bourée, J. Magn. and Magn. Matter., **205**, 184 (1999)

³⁵ A. Llobet, C. Frontera, J. L. Carci-Muñoz, C. Ritter, M. A. G. Aranda, Chem. Mater. **12**, 3648 (2000).

³⁶ R. K. Zheng, C. F. Zhu, J. Q. Xie and X. G. Li, Phys. Rev. B **63** 024427.

³⁷ M. V. Lobanov, A. M. Balagurov, V. Ju. Pomjakushin, P. Fischer, M. Gutmann, A. M. Abakumov, O. G. D'yachenko, E. V. Antipov, O. I. Lebedev, and G. Van Tendeloo, Phys. Rev. B, **61**, 8941 (2000).

³⁸ F. Moussa, M. Hennion, J. Rodriguez-Carvajal, H. Moudeden, L. Pinsard, and A. Revcolevschi, Phys. Rev. B **54**, 15149 (1996); Q. Huang, A. Santoro, J. W. Lynn, R. W. Erwin, J. A. Borchers, J. L. Peng, and R. L. Greene, Phys. Rev. **55**, 14987 (1997).

³⁹ P. Dai, J. Zhang, H. A. Mook, S.-H. Liou, P. A. Dowben, and E. W. Plummer, Phys. Rev. B **54**, R3694, (1996).

⁴⁰ *Statistical Physics Part 1*, Course of Theoretical Physics by L. D. Landau and E. M. Lifshitz, 2nd edition, Pergamon Press.

TABLE II: Selected bond lengths (\AA) and bond angles (deg) for $\text{La}_{1-x}\text{Ca}_x\text{MnO}_3$ ($x = 0.8, 0.85$) samples at $T = 1.6$ and 300 K, calculated according to the structural parameters presented in Table I. At 300 K (1.6 K) the structural model predict one (two) Mn sites. The bond with subscript 'a' denotes bond mainly along the b -axis, while the 'p' stands for bonds in the $a - c$ plane. The table also includes the average bond length $\langle d \rangle = (1/6) \sum_{i=1,6} d_i$, the distortion parameter of the MnO_6 octahedra $s_d^2 = (1/6) \sum_{i=1,6} [(d_i - \langle d \rangle)/\langle d \rangle]^2$.

x	0.8		0.85	
T (K)	300	1.6	300	1.6
Mn-Oa $\times 2$	1.915(1)	-	1.908(1)	-
Mn-Op $\times 2$	1.925(1)	-	1.923(3)	-
Mn-Op $\times 2$	1.912(4)	-	1.908(3)	-
Mn(1)-O1a $\times 2$	-	1.895(1)	-	1.894(1)
Mn(1)-O1p $\times 2$	-	1.886(5)	-	1.887(1)
Mn(1)-O2p $\times 2$	-	1.952(7)	-	1.941(5)
Mn(2)-O2a $\times 2$	-	1.895(1)	-	1.898(1)
Mn(2)-O1p $\times 2$	-	1.920(6)	-	1.909(4)
Mn(2)-O2p $\times 2$	-	1.931(6)	-	1.925(5)
Mn(1)-O1a-Mn(1)	159.3(3)	159.9(5)	160.0(4)	159.8(4)
Mn(2)-O2a-Mn(2)	-	159.7(5)	-	158.3(4)
Mn(2)-O1p-Mn(1)	159.1(2)	157.5(4)	158.3(2)	158.7(3)
Mn(2)-O1p-Mn(1)	-	161.5(3)	-	159.8(5)
La-Op $\times 2$	2.369(6)	-	2.344(6)	-
La-Oa $\times 1$	2.37(1)	-	2.38 (1)	-
La-Op $\times 1$	2.527(6)	-	2.513(6)	-
La-Op $\times 2$	2.610(6)	-	2.583(6)	-
La-Op $\times 2$	2.640(5)	-	2.651(6)	-
La-Op $\times 1$	2.864(6)	-	2.864(6)	-
La-Oa $\times 1$	2.97(1)	-	2.94 (1)	-
La-Op $\times 2$	3.098(6)	-	3.112(6)	-
La(1)-O2p $\times 2$	-	2.374(9)	-	2.36 (1)
La(1)-O2a $\times 1$	-	2.38(1)	-	2.35 (1)
La(1)-O1a $\times 1$	-	2.55 (1)	-	2.50 (1)
La(1)-O1p $\times 2$	-	2.58 (1)	-	2.583(6)
La(1)-O2p $\times 2$	-	2.613(8)	-	2.595(6)
La(1)-O1a $\times 1$	-	2.84 (1)	-	2.87 (1)
La(1)-O2a $\times 1$	-	2.97(1)	-	2.98 (1)
La(1)-O1p $\times 2$	-	3.122(9)	-	3.114(7)
La(2)-O1p $\times 2$	-	2.34 (1)	-	2.370(9)
La(2)-O1a $\times 1$	-	2.39(1)	-	2.38 (1)
La(2)-O2a $\times 1$	-	2.53 (1)	-	2.48 (6)
La(2)-O2p $\times 2$	-	2.57 (1)	-	2.564(7)
La(2)-O1p $\times 2$	-	2.705(6)	-	2.654(7)
La(2)-O2a $\times 1$	-	2.87 (1)	-	2.91 (1)
La(2)-O1a $\times 1$	-	2.96(1)	-	2.95 (1)
La(2)-O2p $\times 2$	-	3.038(9)	-	3.077(7)
$\langle d_1 \rangle$	1.917(2)	1.911(2)	1.913(2)	1.907(2)
$\langle d_2 \rangle$		1.915(2)		1.910(2)
$\langle s_d^2 \rangle \times 10^{-5}$	1.61	44.68	2.6	30.14
$\langle s_d^2 \rangle \times 10^{-5}$		7.95		6.45